Available online at www.sciencedirect.com

jmr&t Journal of Materials Research and Technology

https://www.journals.elsevier.com/journal-of-materials-research-and-technology

Original Article

Microstructure evolution of an artificially aged Al-Zn-Mg-Cu alloy subjected to soft- and hard-steel core projectiles

Muhammad Abubaker Khan[a], *Yangwei Wang*[a,b,*], *Huanwu Cheng*[a,b], *Ghulam Yasin*[c], *Abdul Malik*[a], *Faisal Nazeer*[a], *Tahir Ahmad*[d], *Waheed Qamar khan*[e], *Muhammad Kamran*[d], *Mohamed A. Afifi*[f]

[a] *School of Materials Science and Engineering, Beijing Institute of Technology, Beijing 100081, China*
[b] *National Key Laboratory of Science and Technology on Materials under Shock and Impact, Beijing, 100081, China*
[c] *State Key Laboratory of Chemical Resource Engineering, School of Material Science and Engineering, Beijing University of Chemical Technology, Beijing, 100029, China*
[d] *College of Engineering and Emerging Technology, University of Punjab, Lahore, Pakistan*
[e] *Institute of Advanced Materials, Bahauddin Zakariya University, 60800, Multan, Pakistan*
[f] *Brunel Centre for Advanced Solidification Technology (BCAST), Brunel University London, Uxbridge, UB8 3PH, UK*

ARTICLE INFO

Article history:
Received 12 May 2020
Accepted 17 August 2020
Available online 2 September 2020

Keywords:
Al-Zn-Mg alloy
Perforation channel
Hard steel projectile
Soft steel projectile
Precipitates
ASBs

ABSTRACT

An investigation was conducted to study the effect of soft (220 Hv) and hard (750 Hv) steel projectiles on an Al-Zn-Mg-Cu alloy processed by hot extrusion followed by heat treatment (solid solution treatment at 743 K/1.5 h + ageing treatment at 388 K/24 h). The results show that the hardness of the projectile material can influence on the shape and size of the perforation channel formed after the penetration. The hard steel projectile has longer depth of penetration and the crater front diameter is narrower comparing with the Al alloy after penetration by the soft steel projectile. Adiabatic shear bands (ASBs) are formed in the perforation channel after penetration with presence of recrystallized grains within these bands. The ASBs are wider after the hard steel projectile penetration with presence of cracks comparing with the ASBs formed after the soft steel projectile penetration. Precipitates are increased in size and overlapped in the perforation channel which are mainly of G.P. zone and η' precipitates. Hardness values of the Al alloy after penetration increase in the upper side of the perforation channel over the middle and end regions of the channel.

1. Introduction

Aluminium (Al) alloys are extensively used in the automobile, aircraft and army industries owed to the high strength to weight ratio [1–6]. In addition, the need for lightweight structural applications is on high demand to reduce the

* *Corresponding author.*
E-mail: wangyangwei@bit.edu.cn (Y. Wang).
https://doi.org/10.1016/j.jmrt.2020.08.076

fuel consumption [7]. For instance, Al-Zn-Mg-Cu alloys are now being used in several weight-critical armour applications [8–10]. The Al alloys are considered as a potential replacement to the heavy weight alloys like steel [11–13]. This is because Al-Zn-Mg-Cu alloys after heat treatments display a good ballistic protection and short depth of penetrations [14]. The fine semi-coherent η' precipitates can provide strengthening after the heat treatments [15,16]. Consequently, it is of interest to characterize and understand the ballistic behaviour of the Al-Zn-Mg-Cu alloys after the heat treatment to extend the make use of the alloy in the armour industrial applications.

Numerous studies investigated the effect of the dynamic impact in the microstructure of the Al alloys [9,17–20]. This includes the evolution of ASBs, texture development, dislocations, and precipitation evolution [21–25]. For example, ASBs were observed after steel and tungsten carbide penetrators in an Al-Mg-Si alloy [26]. The formation of ASBs was resulted from the high strain rate testing and the increase in temperature [21]. In a related study, Goss {011} <100>$_{Al}$ and P {011}<122>$_{Al}$ textures were formed under compression at 3 × 10^3 s^{-1} of an Al-Zn-Mg-Cu alloy suggesting the formation of the ASBs [7]. In another study, the high dislocation density distributed inside the grains were generated by the significant plastic deformation during penetration by armour-piercing bullets in an Al-Mg alloy [27]. Several investigations studied the precipitation behaviour of the Al alloy during the projectile impact [28,29]. For example, it was found in a recent study that coarse precipitates were heterogeneously distributed along the dislocations and the grain boundaries after high strain rate compression at 1 × 10^3 s^{-1} [20]. Dynamic precipitation of very fine η' and η during high strain rate compression occurred where the volume fraction of precipitates increased with increasing the strain [20]. Another study found that dynamic compressive deformation assists the precipitation process through precipitate coalescence and by changing the precipitates orientation [18]. The need for lightweight structural applications is on high demand to reduce the fuel consumption. Thus, more studies are important for a complete understanding the influence of projectile penetration on the microstructure of the Al-Zn-Mg-Cu alloys.

A review shows that limited data are available to date studying the microstructural response of Al-Zn-Mg-Cu alloys after projectile penetration. Accordingly, the present investigation was initiated to examine the microstructural evolution of an Al-Zn-Mg-Cu alloys after penetration by a soft steel and a hard steel projectile.

2. Experimental material and procedures

An Al-Zn-Mg-Cu alloy with a chemical composition (wt.%) of Al-8.2 Zn-2.4 Cu-2.0 Mg-0.06 Fe-0.01 Si-0.12 Zr was prepared using spray forming technique [30]. The spray forming Al alloy was prepared by Haoran Co. Ltd., Jiangsu, China. The spray forming parameters are as follows: the molten alloy was atomized by nitrogen (N_2) at temperatures were from 973 K–1023 K, spray pressure was from 0.6 to 1.0 MPa, rotation speed was from 2–4 mm min^{-1} and the withdraw speed was ~ 45–55 r min^{-1}. Spray formed Al-alloy ingots were then extruded at 703 K and then quenched by water spray

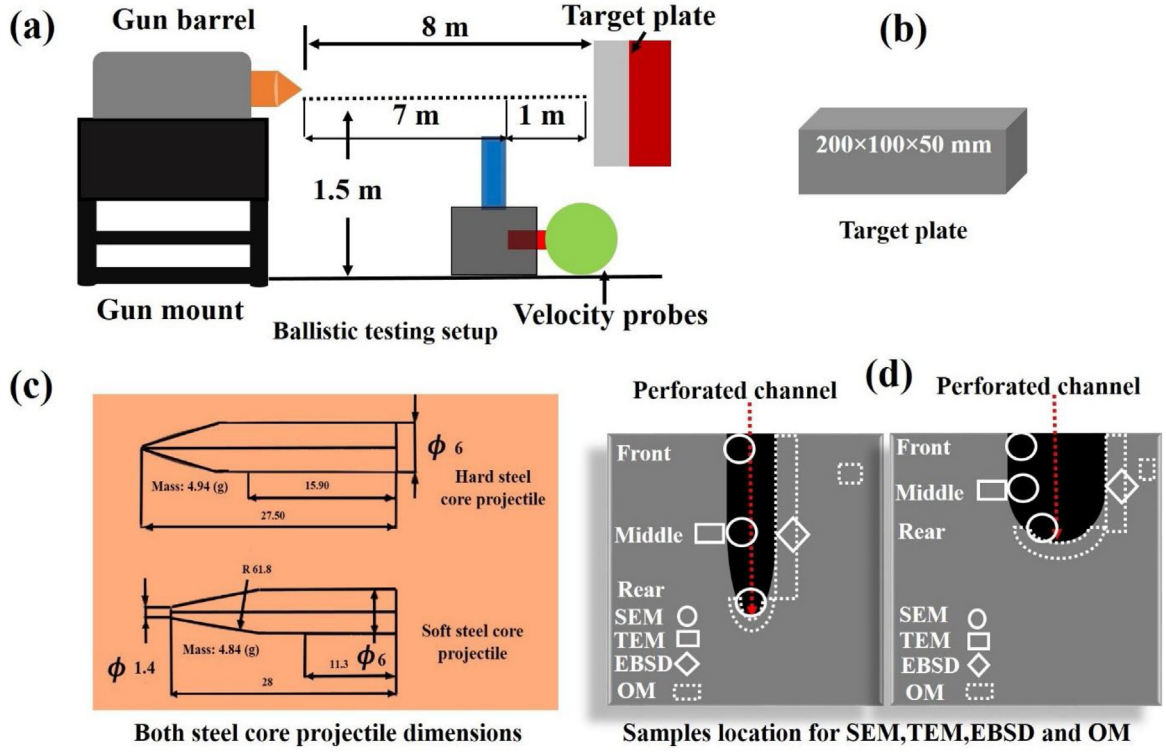

Fig. 1 – (a) schematic drawing of the ballistic testing setup, (b) target plate dimensions, (c) projectile shape with dimensions and (d) SEM, TEM, EBSD and OM samples location from the perforated channel after projectile penetration.

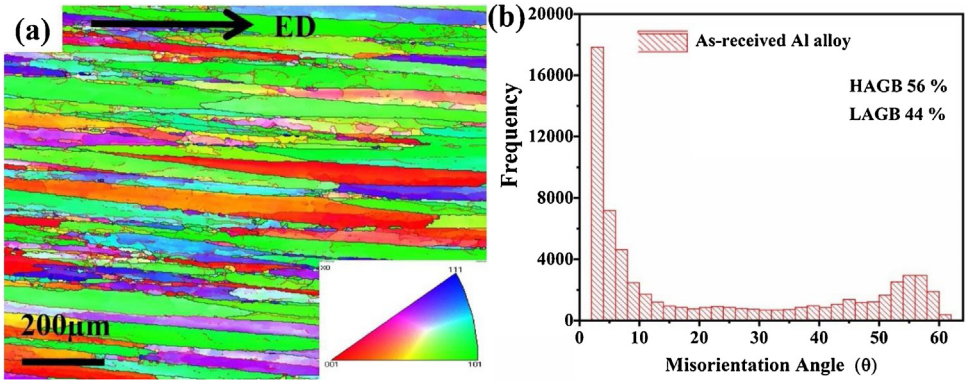

Fig. 2 – (a) EBSD micrograph showing the extrusion direction (ED) and (b) orientation histogram of the as-received Al alloy after the T6 heat treatment.

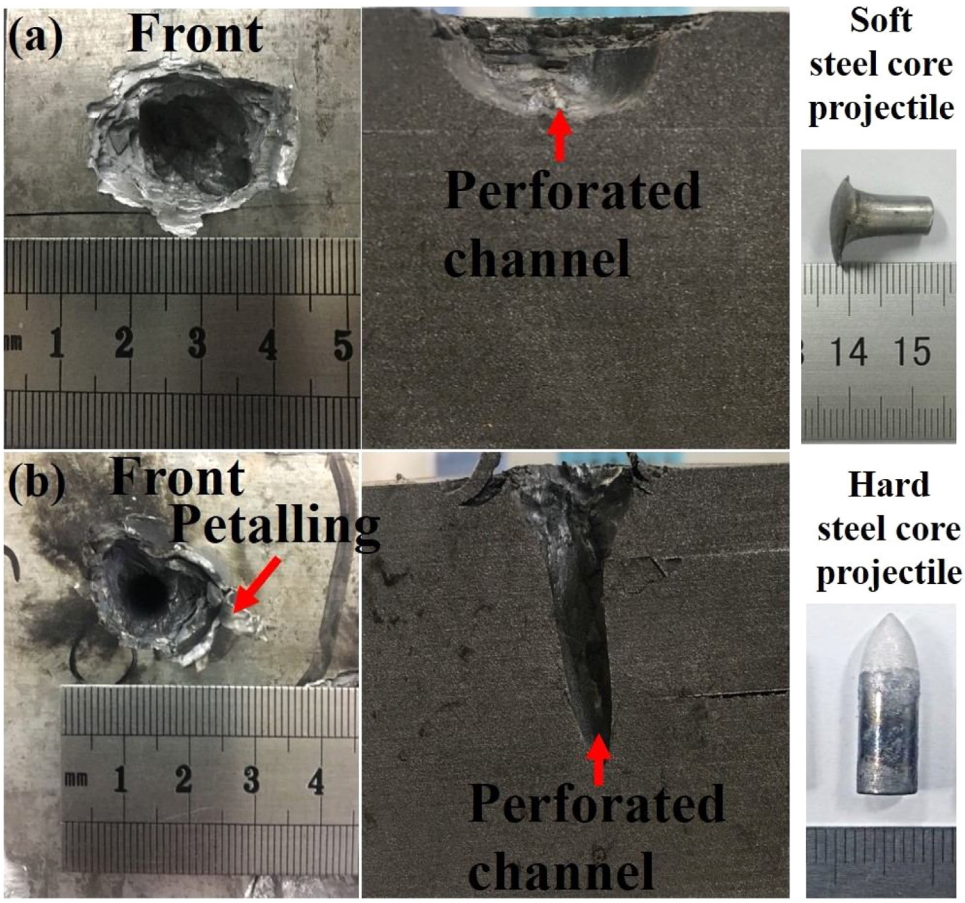

Fig. 3 – The target as-received Al alloy plate showing the perforated channel and the bullets after penetration by: (a) soft steel projectile and (b) hard steel projectile.

at room temperature. Samples produced from spray forming and extrusion are noted as the as-received Al alloy. The as-received Al alloy was then solid solution treated at 743 K/1.5 h followed by the artificial ageing heat treatment (T6) at 388 K/24 h.

The projectile penetration experiment was performed according to the depth of penetration (DOP) test method [17]. The tests were carried out with a soft steel core (~ 220 Vickers hardness) and a hard steel core projectile (~ 750 Vickers hardness) with conical shape using a standard gun barrel. The As-received Al alloy were cut to plates with size of 200 × 100 × 50 mm^3 prior to the ballistic tests. The velocity of the projectile was measured by an infrared light emitting diode photovoltaic cells. The speed of the projectile before penetration was 830 m/s. Three ballistic tests were performed on each target material. A schematic illustration showing the ballistic

Table 1 – Crater front diameter and depth of penetration of the Al alloy after projectile penetration.

Soft steel projectile		Hard steel projectile	
Crater front diameter	Depth of Penetration	Crater front diameter	Depth of Penetration
~ 29 mm	~ 11 mm	~ 17 mm	~ 31 mm

testing setup, target plates and both steel projectile dimensions are displayed in Fig. 1.

The microstructure of the Al alloy was investigated using transmission electron microscopy (TEM), energy dispersive X-ray microanalysis (EDX), electron backscatter diffraction (EBSD), scanning electron microscopy (SEM) and optical microscopy (OM) before and after the projectile penetration experiments. TEM samples were cut near the middle region of the perforation channel as shown in Fig. 1(d) to discs ∅ 3 mm × 0.3 mm and then ground to 0.1 μm foil thickness. Samples were then electro-polished to electron transparency by a mixture of nitric acid and ethanol solution with liquid nitrogen. TEM investigation was carried by Tecnai G^2 F20 TEM. Samples were ground, polished and etched by Keller's reagent for the EBSD, SEM and OM. SEM and EBSD were carried out before and after the projectile penetration using Hitachi S4800 SEM equipped with an HKL-EBSD. Low-angle grains boundaries (LAGBs) were defined from 2 to 15° and high angle grains boundaries (HAGBs) were defined larger than 15°. Micro-hardness test was performed using a LECO 700 AT following the ASTM E140 standard. Micro-hardness test was conducted using Vickers hardness testing machine with a 100 g load and time of 10 s.

3. Results and discussion

3.1. *Microstructure characterization before the projectile penetration*

The microstructure of the Al-Zn-Mg-Cu alloy after the T6 heat treatment was examined and characterized in an earlier report [2]. The precipitates are mainly of η' and η phases with average size of ~ 11 nm [2]. EBSD image of the as-received Al alloy after the T6 heat treatment is displayed in Fig. 2(a) where the grains are elongated in the extrusion direction (ED). The average grain size after the T6 heat treatment was ~ 25 μm. It is apparent from Fig. 2(b) that the as-received alloy after the T6 heat treatment has ~ 56 % of high angle grain boundaries (HAGB's). The presence of HAGB can be owed to dynamic recrystallization during hot extrusion of the Al alloy [31,32].

3.2. *General view after the projectile penetration*

Fig. 3 shows general view of the perforated channel and the bullets after penetration by soft and hard steel projectiles.

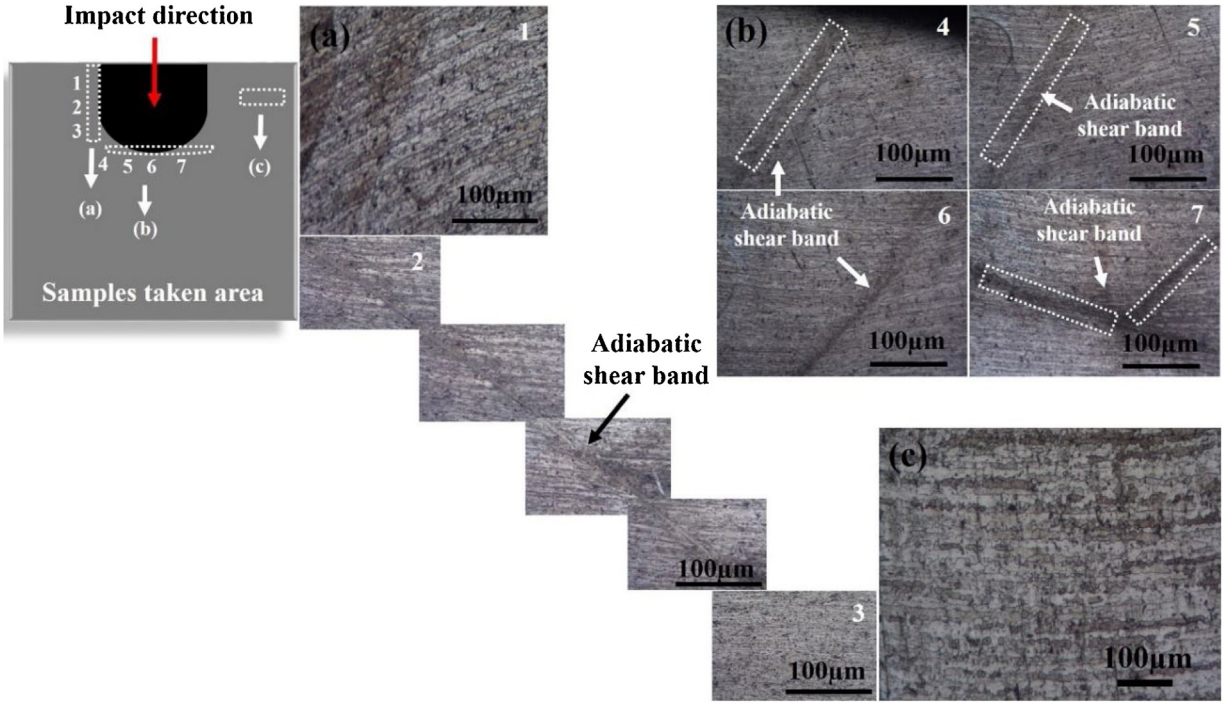

Fig. 4 – OM microstructure evolution of the Al alloy after penetration by a soft steel projectile: (a) side inlet view, (b) bottom inlet view and (c) non-deformed region view.

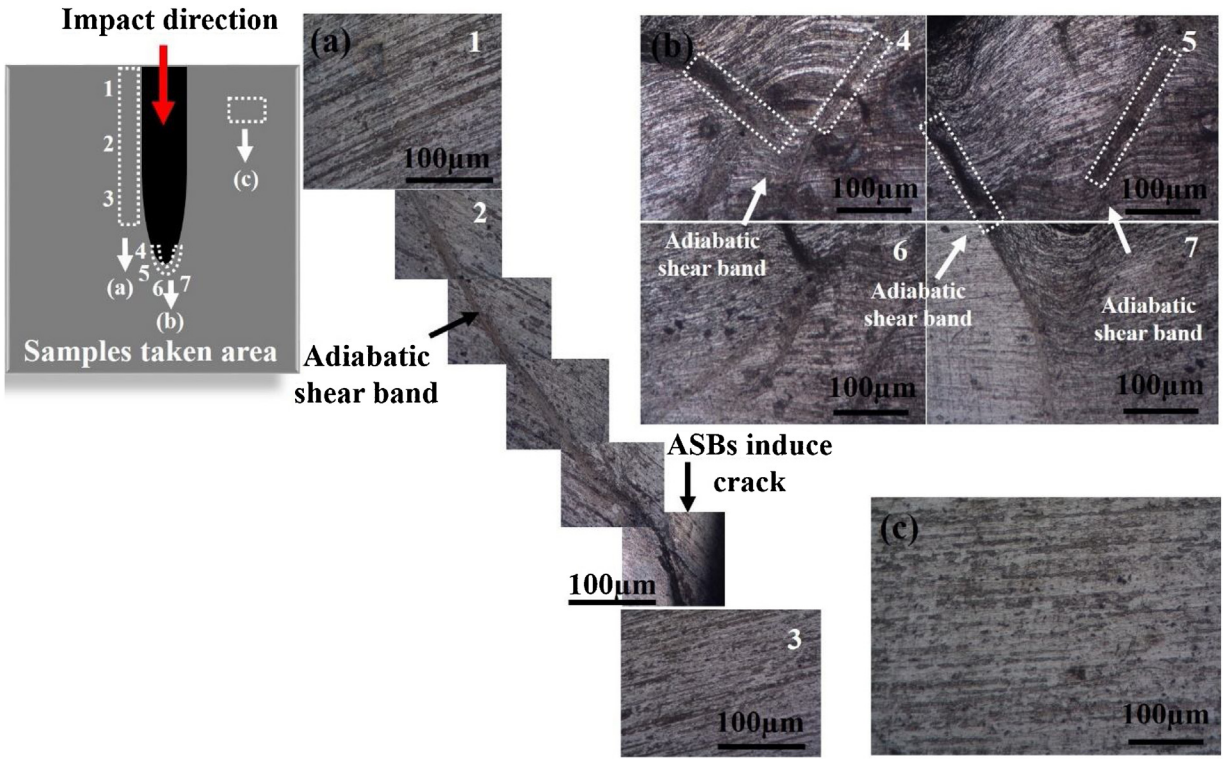

Fig. 5 – OM microstructure evolution of the Al alloy after penetration by a hard steel projectile: (a) side inlet view, (b) bottom inlet view and (c) non-deformed region view.

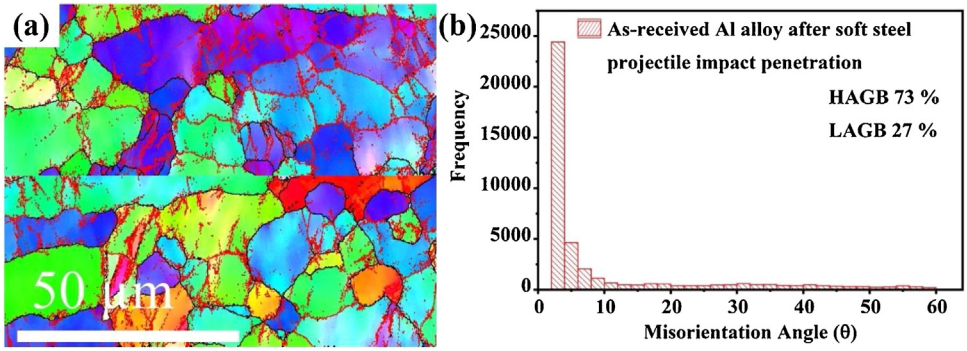

Fig. 6 – (a) EBSD micrograph of the ASB region and (b) orientation histogram of the as-received Al alloy after the T6 heat treatment subjected to soft steel projectile penetration.

It is clearly visible that the projectile hardness can directly affect the perforated channel shape and size after penetration [33–36]. The Al alloy subjected to the hard steel projectile shows longer depth of penetration comparing with the Al alloy subjected to the soft steel projectile. In addition, the crater front diameter is narrower after the hard steel projectile penetration comparing with the carter front diameter formed after the soft steel projectile penetration. The depth of penetration and crater front diameters are summarized in Table 1. The Al alloy in front of the projectile is pushed out with presence of circumferential and radial cracks causing a clear petalling phenomena as observed in Fig. 3 [23]. Petalling phenomena appears as a failure mode when a hemispherical or conical projectile are applied to the material [37]. The impact velocity also plays important role in the formation of petalling on the surface [38]. The projectile speed is high enough to cause petalling and not too high to cause fragmentation in the surface [38,39]. The soft steel projectile was deformed after penetration while the hard steel projectile remained with no deformation which can be resulted to the hardness of the projectile material.

3.3. *Microstructure characterization after projectile penetration*

Fig. 4 shows the OM images from inside the perforation channel after the soft projectile penetration. Grains are deformed and aligned with the projectile direction towards the inlet side

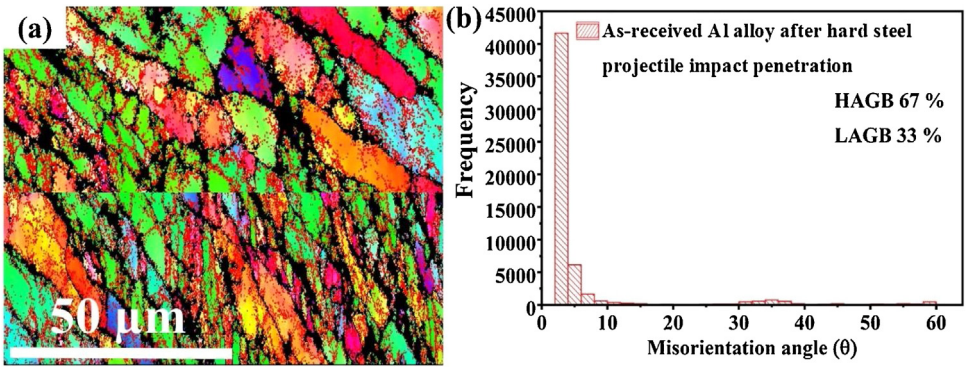

Fig. 7 – (a) EBSD micrograph of the ASB region and (b) orientation histogram of the as-received Al alloy after the T6 heat treatment subjected to hard steel projectile penetration.

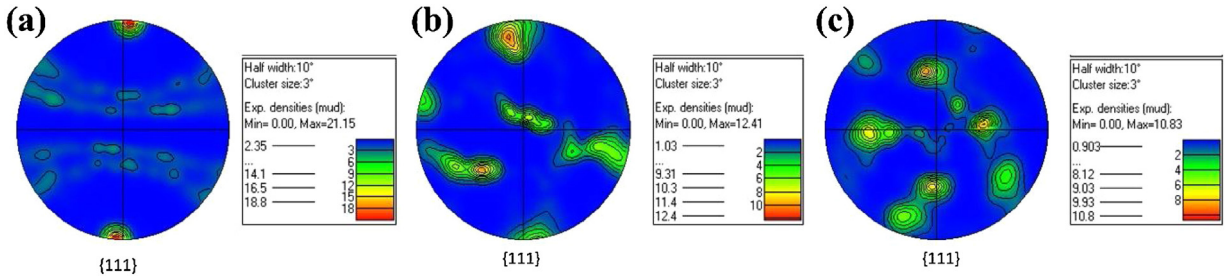

Fig. 8 – Pole figure analysis of the Al alloy where: (a) before projectile penetration (b) after the soft steel projectile penetration and (c) after the hard steel projectile penetration.

as shown in Fig. 4(a-1). The formation of ASBs is observed in Fig. 4(a-2) through the middle region of the perforation channel. No shear cracks are found and the gain structure surrounding the bands are like the nominal Al alloy grains. Fig. 4(a-3) shows fine equiaxed grains in the end of the perforation channel which can be owed to the local dynamic deformation and the temperature rise (623–723 K) during penetration by the projectile [21]. Several micro-ASBs are observed in the bottom side of the perforation channel as displayed in Figs. 4(a 4–7). These bands are formed after high strain rate deformation accompanied with thermal softening [40,41]. No cracks are found in these micro bands with nominal elongated grains surrounding these bands. Fig. 4(c) shows the elongated grains of the non-deformed region. Fig. 5 displays the OM images from inside the perforation channel after the hard projectile penetration. Grains are aligned to the projectile towards the inlet direction like the soft projectile inlet deformed region as displayed in Fig. 5(a-1). The ASBs are formed in the middle of the perforated channel in Fig. 5(a-2) where the band is wider after the hard projectile penetration comparing with the shear bands width after the soft projectile penetration. Cracks are observed in these bands. Fig. 5(a-3) shows fine equiaxed grains as a result of severe deformation. Several micro-ASBs are also found in the rare end of the perforated channel and grains are distorted assisted by severe deformation by the hard projectile penetration as displayed in Fig. 5(b4–7). Fig. 5 (c) shows the nominal elongated grains of the Al alloy in the non-deformed region. It can be concluded that the as-received Al alloy after the T6 heat treatment will fracture after penetration by the hard steel projectile.

It is clearly visible the correlation between the fracture and presence of the ASBs [42]. ASBs are relevant to the stress, strain, strain rate and the temperature during deformation [43,44]. According to Zener and Hollomon model the strain rate can be neglected as it is caused by both strain hardening effect and adiabatic softening effect simultaneously, so the complex effect of strain rate could involve both the hardening and softening effects in target material [45]. The relating shear stress and the strain:

$$\tau = (\tau_o + h\gamma)e^{\left(-\frac{\eta\alpha\gamma}{2\rho c}(2\tau_o + h\gamma)\right)} \quad (1)$$

The rise in temperature and strain:

$$\theta = \frac{1}{\alpha}\left(1 - e^{\left(-\frac{\eta\alpha\gamma}{2\rho c}(2\tau_o + h\gamma)\right)}\right) \quad (2)$$

The critical shear strain of the ASBs:

$$\gamma_c = \frac{\sqrt{\left(\frac{h\rho c}{\gamma\alpha}\right)} - \tau_o}{h} \quad (3)$$

where τ_o is the shear proportion limit ($\tau_o=\sigma_o/2$), h is the coefficient of the strain-strengthening (= 4 GPa), α is the coefficient of thermal softening (= 1/1273 K), η is the coefficient of thermal transition (= 0.9), ρ is the density (= 2840 kgm^{-3}), c is the heat capacity (= 1005 J(Kg°C)$^{-1}$. The corresponding shear stress to form ASBs is 2145 MPa and temperature rise during ASB forma-

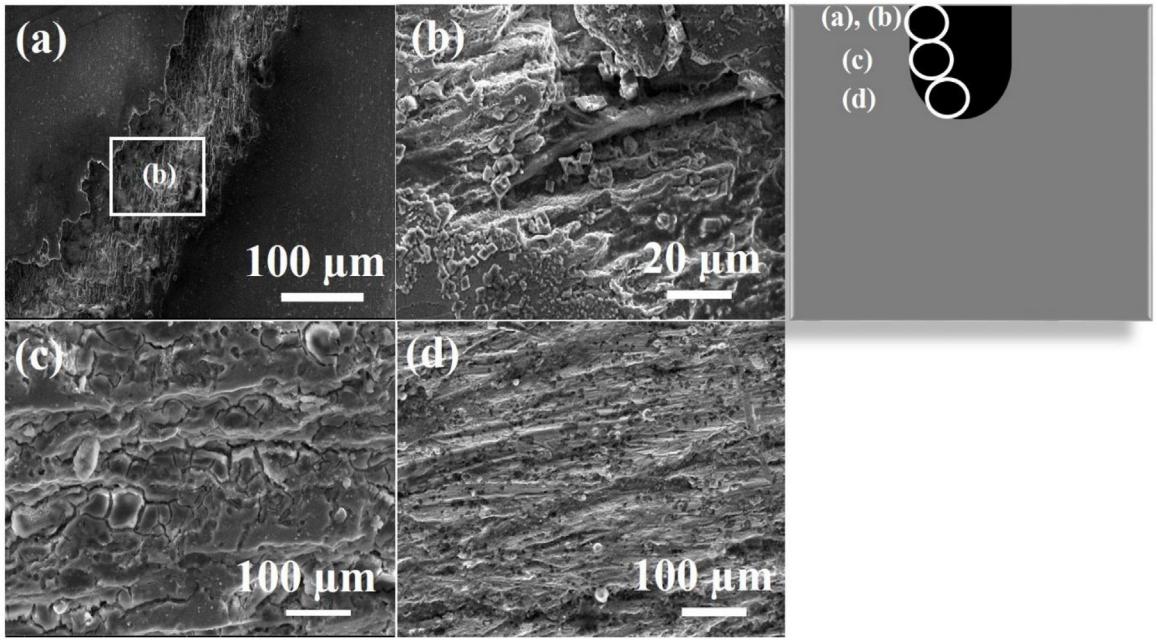

Fig. 9 – The SEM images of the Al alloy after soft steel projectile penetration showing the fracture surface: (a, b) upper side view, (c) middle side view and (d) bottom side view.

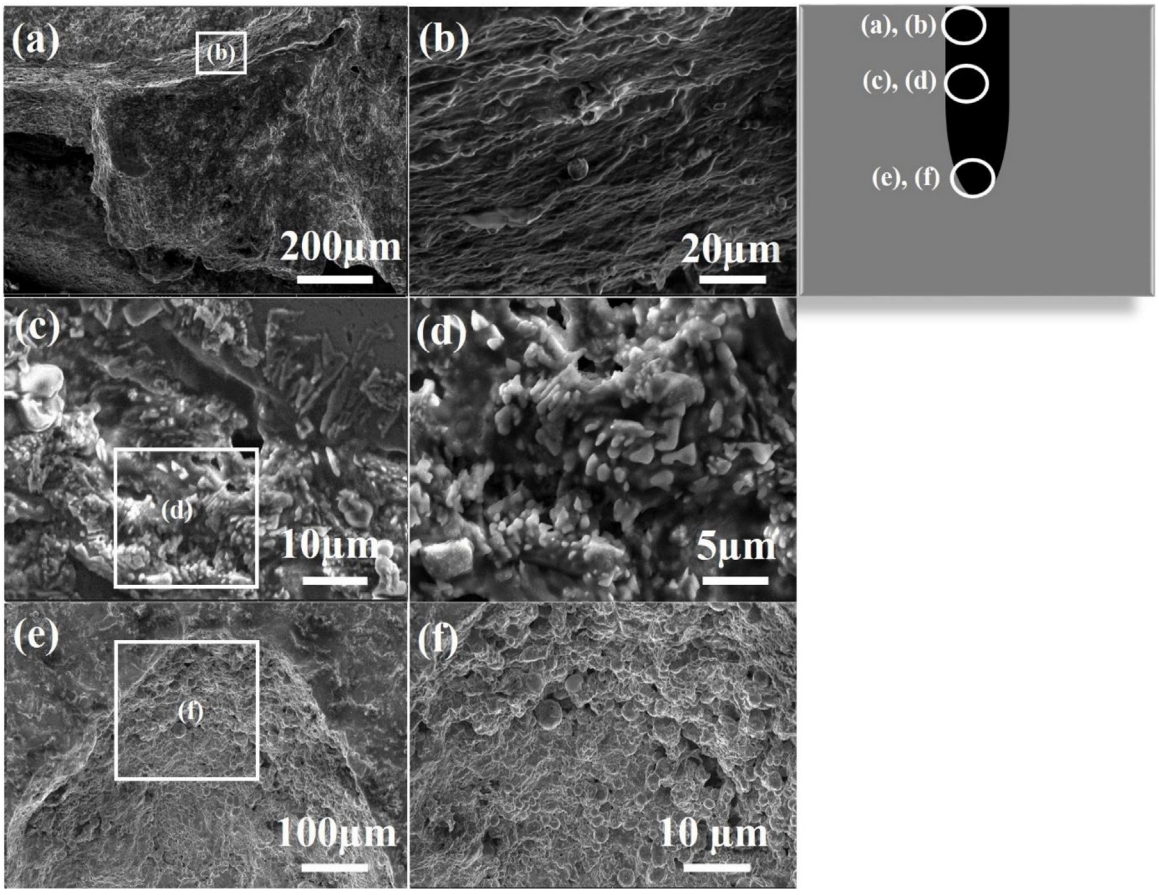

Fig. 10 – The SEM images of the Al alloy after hard steel projectile penetration showing the fracture surface: (a, b) upper side view, (c, d) middle side view and (e, f) bottom side view.

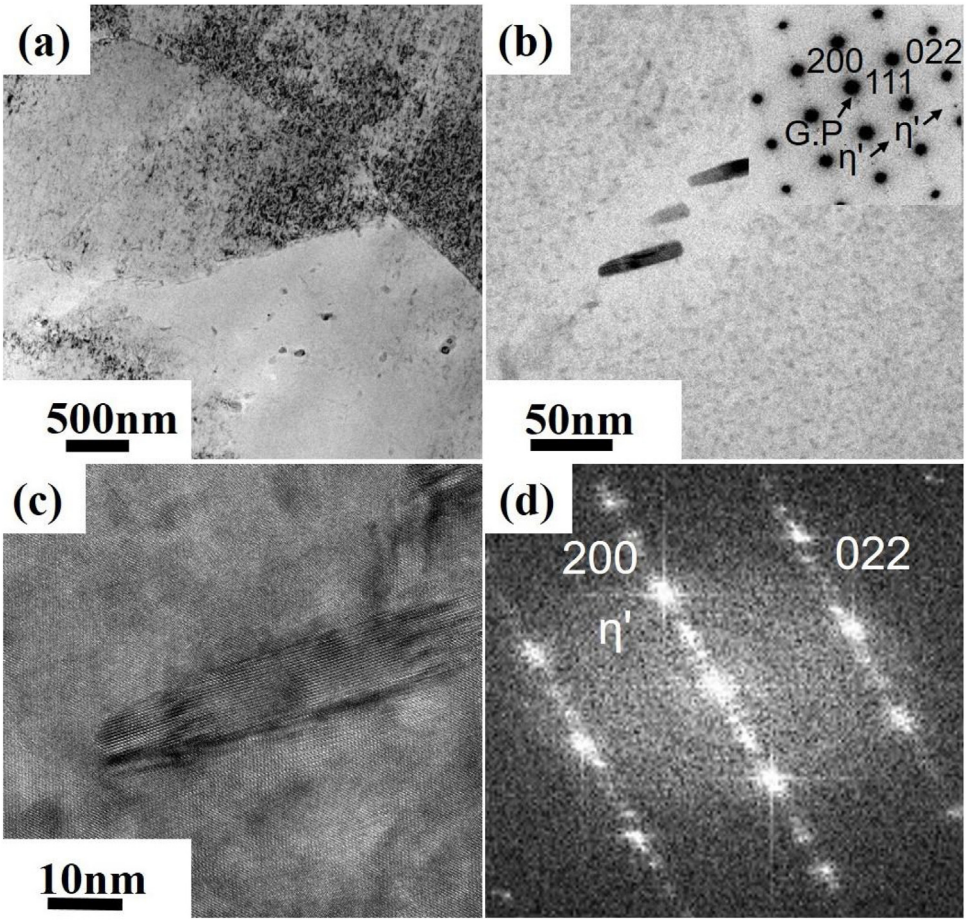

Fig. 11 – TEM micrographs of the Al alloy after the soft steel projectile penetration (a) low magnification, (b) high magnification, (c) HRTEM of a selected precipitate and (d) FFT pattern of the selected precipitate.

tion is 673 K. The high shear in a small region and the rapidly temperature increase leads to dynamic recrystallization and the formation of shear bands [46]. The dynamic recrystallization mechanism in the ASBs caused by projectile penetration is different from the conventional thermoplastic deformation recrystallization. The main difference is the recrystallization process performed in a short period of time. The presence of ASB and fine recrystallized grains in the rare end of the perforation channel support the presence of recrystallization process as depicted in Figs. 4 and 5. The presence of cracks after penetration by hard steel projectile can be resulted from the high shear of the projectile leading to surface tension in the molten Al alloy in the narrow region [47].

Figs. 6 and 7 show the EBSD analysis of the ASB in the middle of the perforation channel after projectile penetration. The elongated grains are fragmented after penetration as displayed in Figs. 6(a) and 7(a). The average grain size in the ASB region after the soft and the hard steel projectile penetration are $\sim$ 11 μm and $\sim$ 7 μm, respectively. The presence of fine grains after the hard projectile penetration can be resulted from the high shear as verified by Fig. 5. The percentage of LAGBs decreases from 73 % after penetration by the soft steel projectile to 67 % after penetration by hard steel projectile, respectively as shown in Figs. 6(b) and 7(b). The fraction of the LAGBs decreases assisted by dynamic recrystallization rate which increased with the high shear [48].

Fig. 8 (a) shows the texture of the Al alloy before the projectile penetration consisting of $\{110\}<111>_{Al}$ shear texture and $\{110\}<113>_{Al}$ and $\{110\}<110>_{Al}$ fiber texture. The texture after the projectiles penetration is mainly of brass and cube texture supporting the presence of dynamic recrystalization [49].

Typical SEM micrographs of the Al alloy after projectiles penetration are displayed in Figs. 9 and 10 showing the hole morphologies after the penetration. Fracture dimples are observed in Fig. 9(a) indicating a ductile fracture mechanism dominate the fracture surface after the soft projectile penetration [50]. Fig. 9(b) shows the dimples in high magnification. Several secondary cracks are found throughout the fracture surface in the middle of the perforated channel as displayed in Fig. 9(c). Cracks are also found in Fig. 9(d) at the end of the perforated channel but with smaller width comparing with the cracks in the middle of the perforated channel. Large area of dimples and surface fragmentation is observed after penetration by the hard projectile as depicted in Fig. 10 (a, b). Fig. 10(b) shows surface fragmentation in high magnification. Several material lacerations, melting and micro cracks are observed in Fig. 10(c), melting and lacerations in higher magnification are in Fig. 10(d) through the middle of the perforated channel.

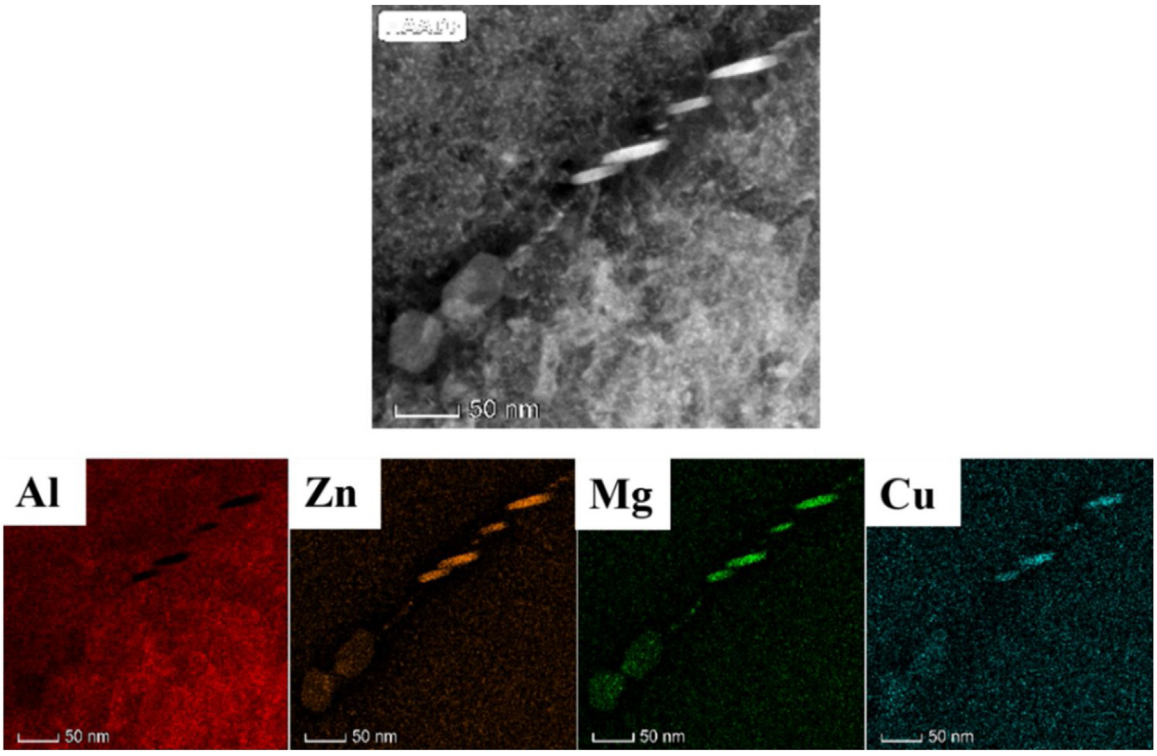

Fig. 12 – EDX mapping of the Al alloy after the soft steel projectile penetration.

Melting surface and solidified region is presented in Fig. 10(e) which owed to the high friction between the projectile and the material surface [26]. Several dimples in the solidified area is displayed in Fig. 10(f).

High number of homogeneously distributed precipitates are observed after the heat treatment of the as-received Al alloy mainly of η' and η precipitates with average size of ~ 11 nm [2]. Fig. 11 shows typical TEM micrographs of the Al alloy after penetration by the soft steel projectile penetration. The microstructure in Fig. 11 (a) displays coarse grains with dislocation tangles within the grains. Grain boundary precipitates are observed in Fig. 11 (b) which are coarse in size having platelet, spherical and overlapped morphologies while fine spherical and platelet precipitates are homogeneously distributed within the grains. The average size of the precipitates in the Al matrix is ~ 25 nm. The precipitates are mainly of G.P. zones and η' precipitates as observed through the SAED pattern along $\{110\}_{Al}$ in Fig. 11 (b). A selected η' precipitate along the Al matrix as verified through the FFT pattern are coherence with the Al matrix as displayed through the HRTEM in Figs. 11 (c, d). Fig. 12 shows an EDX map of the precipitates along the grain boundary after penetration by the soft steel projectile. These precipitates contain percentage of Mg and Zn as displayed in the EDX map with low percentage of Cu. The ratio of Zn: Mg found by EDX was ~ 2:1 which is in agreement with the composition of the phase $MgZn_2$ and the Al-Zn-Mg-Cu phase diagram [51]. Fig. 13 shows typical TEM micrographs of the Al alloy after penetration by the hard steel projectile. Sub-grains are observed with high dislocation tangles within the original coarse grains as displayed in Fig. 13 (a). Platelet coarse precipitates are observed along dislocations and grain boundaries with presence of fine precipitates within the grains having average size ~ 35 nm, mainly of G.P. zones and η' precipitates as shown in Fig.13 (b). Fig. 13 (c, d) presents three fine precipitates where first precipitate is for η' phase and the other precipitates are a G.P. zone and η' phase as verified by the FFT patterns. There is no mismatch of the lattice planes between the GP zone and the Al matrix in region 1, supporting the coherency between these phases while there is mismatch between the G.P. zone and the η' precipitate as presented in region 2 in Fig. 13 (c, d). The presence of two precipitates incoherent to each other can be resulted from the overlapping of precipitates where the G.P. zone nucleated close to the η' precipitate and with growing got overlapped [2,52]. Selected precipitates in Fig. 14 along the grain boundaries after penetration by the hard steel projectile showing similar observations as after penetration by the soft steel projectile penetration where the ratio of Zn: Mg ~ 2:1 with presence of low percentage of Cu. The increase in the size of precipitates in the perforation channel region after penetration by the hard steel projectile can be resulted from the high shear in the area [18,53]. The precipitates increase in size after penetration by the hard projectile because of the high shear as verified in Fig. 13.

3.4. *Hardness (H_v) after projectiles penetration*

The average hardness values of the Al alloy before the projectile penetration is ~ 240 HV taken from 10 mm distance from the projectile penetration point. The hardness variation from the impact surface towards outside after the projectile penetration by the soft and the hard steel projectiles is

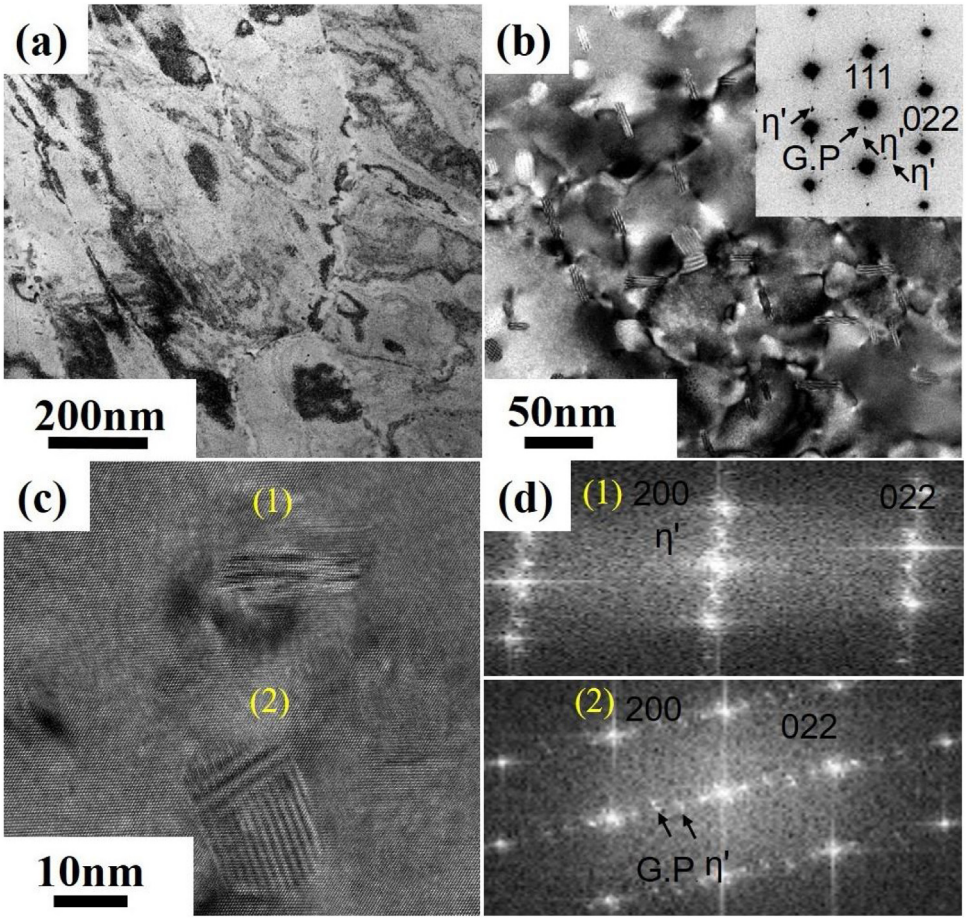

Fig. 13 – TEM micrographs of the Al alloy after hard steel projectile penetration: (a) low magnification, (b) high magnification, (c) HRTEM of two selected precipitates and (d) FFT pattern of the selected precipitates.

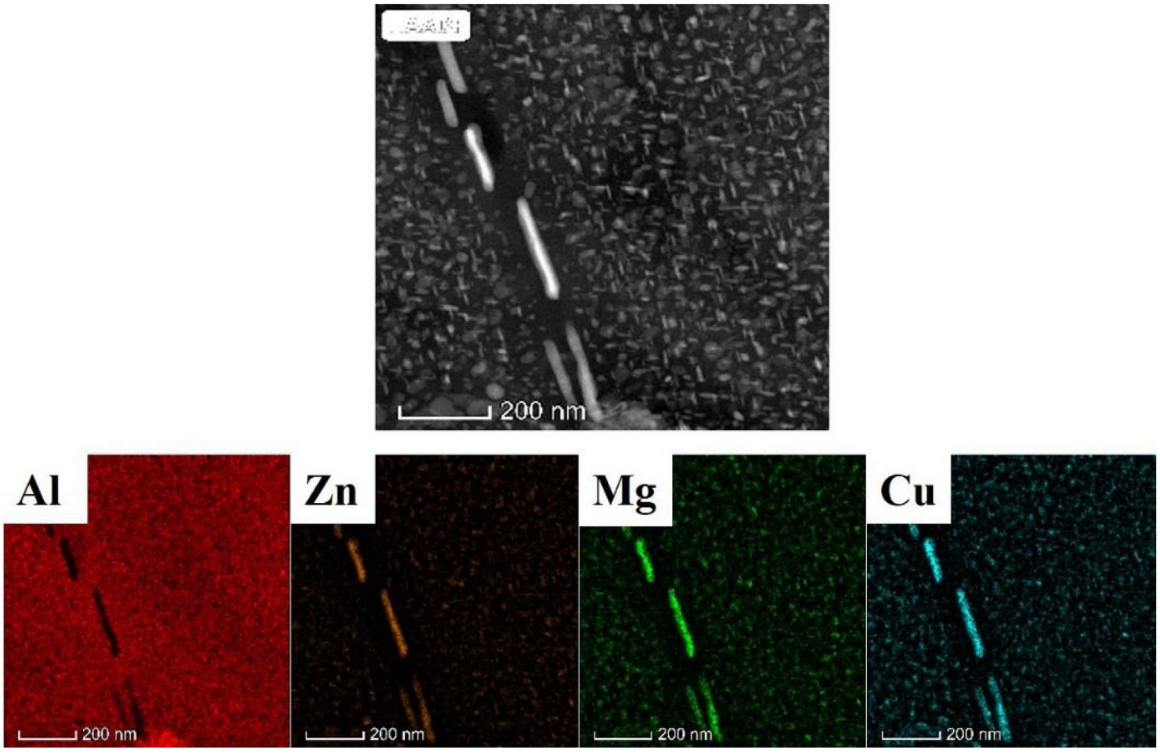

Fig. 14 – EDX mapping of the Al alloy after the hard steel projectile penetration.

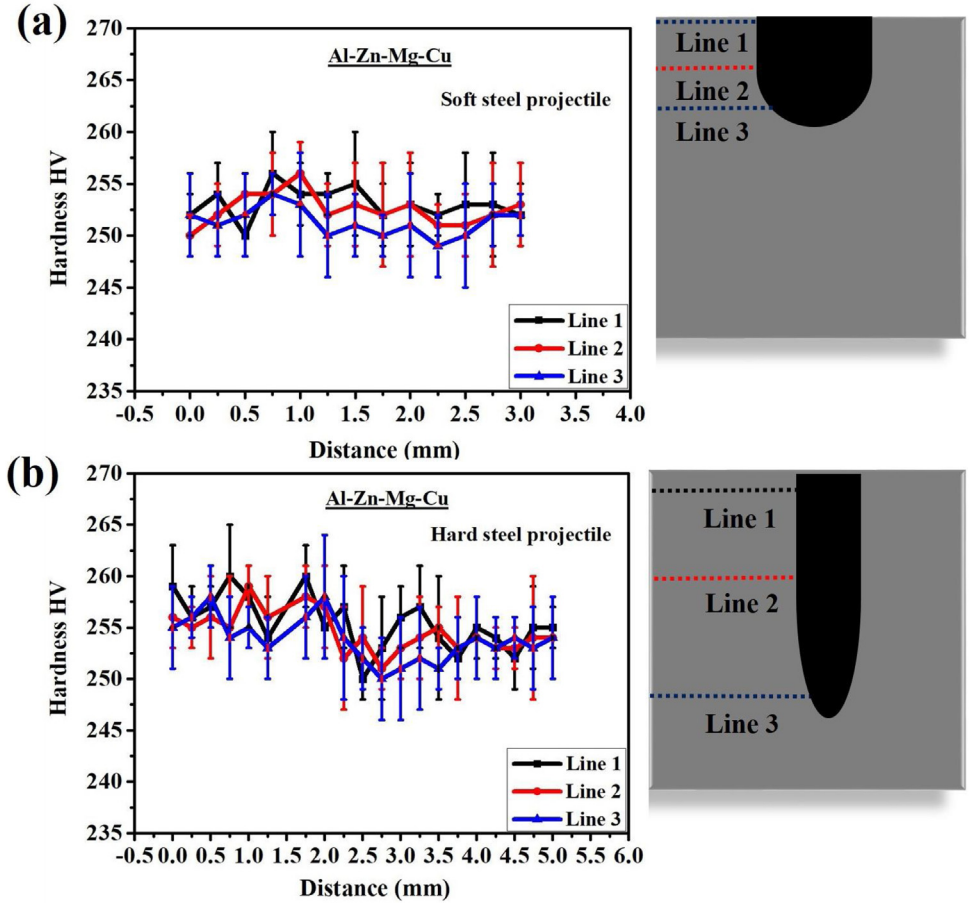

Fig. 15 – The hardness of Al alloy after penetration by: (a) soft steel projectile and (b) hard steel projectile.

shown in Fig. 15. Hardness values in Fig. 15(a and b) show that the upper side of the perforation channel have higher values than the middle and the end regions of the channel. The rise in the hardness values in the upper area owes to the local deformation in the area while the drop in the bottom region areas can be owed to the crack formation after the soft projectile penetration and melting after the hard projectile penetration. The local deformation leads to the increase in the dislocation tangles and the number of precipitates as verified in Figs. 11 and 13. The hardness values in the perforation channel after the hard projectile penetration is higher comparing with the hardness values in the channel after the soft projectile penetration. The rise in hardness owes to the large number of precipitates mainly of G.P. zones and η' precipitates as presented in Fig. 13. The decrease in hardness with increasing the distance from the perforation channel resulted from the decrease of the dislocation density to the nominal Al alloy [2].

4. Summary and conclusions

1 An Al-Zn-Mg-Cu alloy processed by spray forming and extrusion followed by T6 artificial ageing heat treatment was subjected to soft and hard steel core projectiles leading to the formation of a perforation channel. The high shear provided by the hard steel projectile increases the width of the ASBs and leading to the presence of micro-cracks. The high shear and the rise in temperature in a narrow region lead to recrystallization and grain refinement.

2 The high shear provided by the steel projectile penetration assists the precipitation process through dynamic precipitation. No change in the precipitate's composition or orientation in the perforation region after projectile penetration.

3 Hardness values are high in the upper side of the perforation channel after projectiles penetration due to the presence of high dislocations and large number of precipitates. The crack formation after the soft projectile and melting after the hard projectile penetration lead to the drop in the hardness values in the middle and end regions of the channel. The hardness values in the perforation channel after the hard projectile penetration is higher comparing with the hardness values after the soft projectile penetration because of the large number of precipitates.

Conflicts of interest

The authors declare no conflicts of interest.

Acknowledgments

This project is financially supported by the National Key Laboratory Foundation of China. We are thankful to "Jiangsu Haoran Spray Forming Alloy CO., LTD., Jiangsu, 212009, PR China, for providing spray formed Al-Zn-Mg-Cu alloy.

REFERENCES

[1] Khan MA, Wang Y, Anjum MJ, Yasin G, Malik A, Nazeer F, et al. Effect of heat treatment on the precipitate behaviour, corrosion resistance and high temperature tensile properties of 7055 aluminum alloy synthesis by novel spray deposited followed by hot extrusion. Vacuum 2020;174:109185.
[2] Khan MA, Wang Y, Afifi MA, Malik A, Nazeer F, Yasin G, et al. Microstructure and mechanical properties of an Al-Zn-Cu-Mg alloy processed by hot forming processes followed by heat treatments. Mater Charact 2019;157:109901.
[3] Zhang W, Chen X, Zhuo B, Li P, He L. Effect of strain rate and temperature on dynamic mechanical behavior and microstructure evolution of ultra-high strength aluminum alloy. Mater Sci Eng A 2018;730:336–44.
[4] Chen Y, Pedersen K, Clausen A, Hopperstad O. An experimental study on the dynamic fracture of extruded AA6xxx and AA7xxx aluminium alloys. Mater Sci Eng A 2009;523(1-2):253–62.
[5] Afifi MA, Wang YC, Pereira PHR, Huang Y, Wang Y, Cheng X, et al. Effect of heat treatments on the microstructures and tensile properties of an ultrafine-grained Al-Zn-Mg alloy processed by ECAP. J Alloys Compd 2018;749:567–74.
[6] Khan MA, Wang Y, Yasin G, Malik A, Nazeer F, Khan WQ, et al. Microstructure characteristic of spray formed 7055 Al alloy subjected to ballistic impact by two different steel core projectiles impact. J Mater Res Technol 2019;8(6):6177–90.
[7] Ku AY, Khan AS, Gnäupel-Herold T. Quasi-static and dynamic response, and texture evolution of two overaged Al 7056 alloy plates in T761 and T721 tempers: experiments and modeling. Int J Plast 2020:102679.
[8] Fras T, Colard L, Lach E, Rusinek A, Reck B. Thick AA7020-T651 plates under ballistic impact of fragment-simulating projectiles. Int J Impact Eng 2015;86:336–53.
[9] Mishra B, Mondal C, Goyal R, Ghosal P, Kumar KS, Madhu V. Plastic flow behavior of 7017 and 7055 aluminum alloys under different high strain rate test methods. Mater Sci Eng A 2014;612:343–53.
[10] Khan MA, Wang Y, Yasin G, Nazeer F, Malik A, Khan WQ, et al. The effect of strain rates on the microstructure and the mechanical properties of an over-aged Al-Zn-Mg-Cu alloy. Mater Charact 2020;167:110472.
[11] Holmen JK, Johnsen J, Jupp S, Hopperstad OS, Børvik T. Effects of heat treatment on the ballistic properties of AA6070 aluminium alloy. Int J Impact Eng 2013;57:119–33.
[12] Børvik T, Olovsson L, Dey S, Langseth M. Normal and oblique impact of small arms bullets on AA6082-T4 aluminium protective plates. Int J Impact Eng 2011;38(7):577–89.
[13] Khan MA, Wang Y, Cheng H, Nazeer F, Yasin G, Farooq MU, et al. Ballistic behaviour of spray formed AA7055 aluminum alloy against tungsten core projectile impact. Vacuum 2019;159:482–93.
[14] Mondal C, Mishra B, Jena PK, Siva Kumar K, Bhat TB. Effect of heat treatment on the behavior of an AA7055 aluminum alloy during ballistic impact. Int J Impact Eng 2011;38(8):745–54.
[15] Gjønnes J, Simensen CJ. An electron microscope investigation of the microstructure in an aluminium-zinc-magnesium alloy. Acta Metall 1970;18(8):881–90.
[16] Srivatsan TS, Sriram S, Veeraraghavan D, Vasudevan V. Microstructure, tensile deformation and fracture behaviour of aluminium alloy 7055. J Mater Sci 1997;32(11): 2883–94.
[17] Khan MA, Wang Y, Malik A, Nazeer F, Yasin G, Khan WQ, et al. Microstructure characterization of 7055-T6, 6061-T6511 and 7A52-T6 Al alloys subjected to ballistic impact against heavy tungsten alloy projectile. Arch Civ Mech Eng 2019;19(4):1484–96.
[18] Afifi MA, Pereira PHR, Wang YC, Wang Y, Li S, Langdon TG. Effect of ECAP processing on microstructure evolution and dynamic compressive behavior at different temperatures in an Al-Zn-Mg alloy. Mater Sci Eng A 2017;684:617–25.
[19] Yang Q, Deng Z, Zhang Z, Liu Q, Jia Z, Huang G. Effects of strain rate on flow stress behavior and dynamic recrystallization mechanism of Al-Zn-Mg-Cu aluminum alloy during hot deformation. Mater Sci Eng A 2016;662:204–13.
[20] Afifi MA, Wang YC, Langdon TG. Effect of dynamic plastic deformation on the microstructure and mechanical properties of an Al–Zn–Mg alloy. Mater Sci Eng A 2020:139287.
[21] Khan MA, Wang Y, Yasin G, Nazeer F, Malik A, Ahmad T, et al. Adiabatic shear band localization in an Al–Zn–Mg–Cu alloy under high strain rate compression. J Mater Res Technol 2020.
[22] Yang Y, Zheng HG, Shi ZJ, Zhang QM. Effect of orientation on self-organization of shear bands in 7075 aluminum alloy. Mater Sci Eng A 2011;528(6):2446–53.
[23] Zhang B, Jiang J-T, Liu L, Shao W-Z, Zhen L. Texture evolution and recrystallization mechanism in a Mg–3Al–1Zn alloy under ballistic impact. J Alloys Compd 2020;816:152599.
[24] Wu Y, Liao H, Lü C. Dynamic precipitation and recrystallization in Al-12.5 wt%Si-0.6 wt%Mg-0.1 wt%Ti alloy during hot-rolling and their impacts on mechanical properties. J Alloys Compd 2019;788:125–35.
[25] He H, Wu X, Sun C, Li L. Grain structure and precipitate variations in 7003-T6 aluminum alloys associated with high strain rate deformation. Mater Sci Eng A 2019;745: 429–39.
[26] Manes A, Pagani M, Saponara M, Mombelli D, Mapelli C, Giglio M. Metallographic characterisation of Al6061-T6 aluminium plates subjected to ballistic impact. Mater Sci Eng A 2014;608:207–20.
[27] Jung J, Cho YJ, Kim S-H, Lee Y-S, Kim H-J, Lim C-Y, et al. Microstructural and mechanical responses of various aluminum alloys to ballistic impacts by armor piercing projectile. Mater Charact 2020;159:110033.
[28] Cardoso KR, Travessa DN, Botta WJ, Jorge AM. High strength AA7050 Al alloy processed by ECAP: microstructure and mechanical properties. Mater Sci Eng A 2011;528(18):5804–11.
[29] Deschamps A, Fribourg G, Bréchet Y, Chemin JL, Hutchinson CR. In situ evaluation of dynamic precipitation during plastic straining of an Al–Zn–Mg–Cu alloy. Acta Mater 2012;60(5):1905–16.
[30] Liu LL, Pan QL, Wang XD, Xiong SW. The effects of aging treatments on mechanical property and corrosion behavior of spray formed 7055 aluminium alloy. J Alloys Compd 2018;735:261–76.
[31] Ke D, Hengcheng L, Qiumin J, Yun T. Effect of hot extrusion on mechanical properties and microstructure of near eutectic Al–12.0% Si–0.2% Mg alloy. Mater Sci Eng A 2010;527(26):6887–92.
[32] Jazaeri H, Humphreys F. The transition from discontinuous to continuous recrystallization in some aluminium alloys: I–the deformed state. Acta Mater 2004;52(11):3239–50.

[33] Xiao X, Zhang W, Wei G, Mu Z. Effect of projectile hardness on deformation and fracture behavior in the Taylor impact test. Mater Des 2010;31(10):4913–20.
[34] Børvik T, Dey S, Clausen AH. Perforation resistance of five different high-strength steel plates subjected to small-arms projectiles. Int J Impact Eng 2009;36(7):948–64.
[35] Chen XW, Huang XL, Liang GJ. Comparative analysis of perforation models of metallic plates by rigid sharp-nosed projectiles. Int J Impact Eng 2011;38(7):613–21.
[36] Chen XW, Li QM. Perforation of a thick plate by rigid projectiles. Int J Impact Eng 2003;28(7):743–59.
[37] Wierzbicki T. Petalling of plates under explosive and impact loading. Int J Impact Eng 1999;22(9-10):935–54.
[38] Szymczak T, Makowska K, Kowalewski ZL, Lasota P. An influence of impact energy on magnesium alloy behaviour. Int J Mech Mater Des 2019:1–15.
[39] Piekutowski AJ. Holes produced in thin aluminum sheets by the hypervelocity impact of aluminum spheres. Int J Impact Eng 1999;23(1):711–22.
[40] Lee W-S, Sue W-C, Lin C-F, Wu C-J. The strain rate and temperature dependence of the dynamic impact properties of 7075 aluminum alloy. J Mater Process Technol 2000;100(1):116–22.
[41] Owolabi GM, Odeshi AG, Singh MNK, Bassim MN. Dynamic shear band formation in Aluminum 6061-T6 and Aluminum 6061-T6/Al2O3 composites. Mater Sci Eng A 2007;457(1):114–9.
[42] Lee CG, Lee Y-J, Lee S. Observation of adiabatic shear bands formed by ballistic impact in aluminum-lithium alloys. Scr Metall Mater 1995;32(6):821–6.
[43] Xu YB, Zhong WL, Chen YJ, Shen LT, Liu Q, Bai YL, et al. Shear localization and recrystallization in dynamic deformation of 8090 Al–Li alloy. Mater Sci Eng A 2001;299(1):287–95.
[44] Li Q, Xu YB, Lai ZH, Shen LT, Bai YL. Dynamic recrystallization induced by plastic deformation at high strain rate in a Monel alloy. Mater Sci Eng A 2000;276(1):250–6.
[45] De Maddis M, Russo Spena P. Plastic flow behavior of twinning induced plasticity steel from low to warm temperatures. J Mater Res Technol 2020;9(2):1708–19.
[46] Gil Sevillano J, van Houtte P, Aernoudt E. Large strain work hardening and textures. Prog Mater Sci 1980;25(2):69–134.
[47] Christman T, Shewmon PG. Adiabatic shear localization and erosion of strong aluminum alloys. Wear 1979;54(1):145–55.
[48] Pereira PHR, Wang YC, Huang Y, Langdon TG. Influence of grain size on the flow properties of an Al-Mg-Sc alloy over seven orders of magnitude of strain rate. Mater Sci Eng A 2017;685:367–76.
[49] Chen Y, Yang Y, Feng Z, Huang B, Luo X. Surface gradient nanostructures in high speed machined 7055 aluminum alloy. J Alloys Compd 2017;726:367–77.
[50] Kobayashi T. Strength and fracture of aluminum alloys. Mater Sci Eng A 2000;280(1):8–16.
[51] Marlaud T, Deschamps A, Bley F, Lefebvre W, Baroux B. Evolution of precipitate microstructures during the retrogression and re-ageing heat treatment of an Al–Zn–Mg–Cu alloy. Acta Mater 2010;58(14):4814–26.
[52] Afifi MA, Wang YC, Pereira PHR, Huang Y, Wang Y, Cheng X, et al. Mechanical properties of an Al-Zn-Mg alloy processed by ECAP and heat treatments. J Alloys Compd 2018;769:631–9.
[53] Li Z-h, Xiong B-q, Zhang Y-a, Zhu B-h, Wang F, Liu H-w. Microstructural evolution of aluminum alloy 7B04 thick plate by various thermal treatments. Trans Nonferrous Met Soc China 2008;18(1):40–5.